Correlation and spectrum of dust acoustic waves in a radio-frequency plasma using PK-4 on the International Space Station

J. Goree and Bin Liu*
Department of Physics and Astronomy, The University of Iowa, Iowa City, Iowa 52242, USA

M. Y. Pustylnik and H. M. Thomas
Institut für Materialphysik im Weltraum, Deutsches Zentrum für Luft- und Raumfahrt, Münchener Straße 20, 82234 Weßling, Germany

V. E. Fortov, A. M. Lipaev, V. I. Molotkov,† A. D. Usachev, and O. F. Petrov
Joint Institute for High Temperatures, Russian Academy of Sciences, Izhorskaya 13/19, 125412 Moscow, Russia

M. H. Thoma
I. Physikalisches Institut, Justus-Liebig-Universität Gießen, Heinrich-Buff-Ring 16, 35392 Gießen, Germany

E. Thomas Jr and U. Konopka
Physics Department, Auburn University, Auburn, Alabama 36849,USA

S. Prokopiev
Gagarin Research and Test Cosmonaut Training Center, 141160 Star City, Moscow Region, Russia
(Dated: October 15, 2020)

Dust acoustic waves were investigated in an experiment under microgravity conditions, using the European Space Agency-Roscosmos facility PK-4 on the International Space Station (ISS). A three-dimensional dust cloud was confined in a glow-discharge plasma powered by a radio-frequency coil in low-pressure neon gas. Low-frequency dust acoustic waves (DAWs) were spontaneously excited, due to the flowing ions in the plasma. Dust motion was imaged using video cameras, yielding the position for individual dust particles. Besides these particle-level measurements, the dust was also measured as a fluid continuum, to obtain its velocity and density fluctuations. A space-time diagram of the dust-fluid velocity reveals that the waves changed properties as they propagated across the dust cloud, in the direction of the ion flow. Density fluctuations were characterized by a wave spectrum, indicating the emergence of collective vibration modes in a broad range of wave numbers. The decay of the modes was characterized by density correlation functions. Fitting the correlation functions to an analytical model yields an experimental measurement of the dispersion relation for DAWs, which is compared to that from a linear theory.

I. INTRODUCTION

Waves have long been a topic of study in dusty plasmas, which contain electrons, ions, gas atoms, and charged dust particles [1–5]. These four-component mixtures allow a study of waves at microscopic particle level, to reveal lattice waves [6–9] or phonons [10, 11] arising from the random motion of dust particles. Dusty plasmas also exhibit rich phenomena at macroscopic levels. Particularly, a low-frequency sound wave due to the collective effect of ions, electrons and dust can propagate through the dust component; this wave is the so-called dust acoustic wave (DAW) [12–17], analogous to the ion acoustic wave. One peculiar feature of the DAW is that it can be spontaneously excited due to flowing ions streaming pass the dust particles. The DAW has been observed in dusty plasma experiments under ground-based [18–45] and microgravity conditions using parabolic flights [46–49] and the International Space Station (ISS) [50–55].

Experiments under microgravity conditions are of great importance in the field of dusty plasma. Microgravity conditions allow dust to fill a large three-dimensional volume, which is very helpful for a study of the physics in three dimensions. In the past decades, several microgravity facilities have been developed; these include the International Plasma Microgravity Facility (IMPF) [46] for parabolic flight experiments, and the PKE-Nefedov [56], PK-3 Plus [57], and Plasma-Kristall 4 (PK-4) [58, 59] on board the ISS. Under microgravity conditions, the DAW was observed to self-excite in bulk plasmas and to propagate many wavelengths [54].

Here, we report an experiment performed using the PK-4 instrument on board the ISS. This instrument features an elongated discharge chamber that can be powered by DC or radio-frequency (RF) voltages. The elongated chamber is particularly suitable to study wave propagation. In a previous experiment on the ISS [54, 55], the DAW was investigated in a DC plasma, with a drifting dust cloud that was tracked for about 10 s. Our

* Corresponding author: bin-liu@uiowa.edu
† Our dear colleague Vladimir Ivanovich Molotkov passed away unexpectedly on July 11, 2019.

experiment presented here differs from this previous experiment; the dust cloud in our experiment was confined in an RF plasma. Our observed waves were long-lived; they were sustained at a steady amplitude over time.

We will explore the emergence of collective modes arising from density fluctuations, over a broad range of wave numbers. Thermal motion of particles in a dusty plasma has been demonstrated, under some conditions [10, 11], to correspond to a broadband spectrum of incoherent modes, often described as a phonon spectrum. Aside from thermal motion, however, there can also be collective motion arising from instabilities, and this can result in a spectrum with a narrower bandwidth, corresponding to modes where the wave numbers are most unstable. In our system, however, DAWs are expected to be excited in a narrow bandwidth, due to an instability driven by ion flow. Here we investigate a spectrum of modes that is observed in the presence of not only this instability, but also nonlinear coupling. Such waves may be expected to exhibit temporal decay, which will be characterized by a correlation function.

II. EXPERIMENT

Our experiment was performed using the Joint ESA-Roscosmos "Experiment Plasma kristall-4" (PK-4), which is a facility on board the ISS [58, 59]. Figure 1(a) shows a sketch of some features that were used in this experiment. In the experiment, the U-shaped glass plasma chamber was initially powered at a DC voltage, through the active and passive electrodes. A DC discharge was established in the chamber, which was filled with 35-Pa neon gas. At a later time, the RF coil was powered by radio-frequency (RF) voltages at 88 MHz, generating a RF plasma near the center of the chamber. The dust particles, which had a radius of 3.43 μm, were momentarily injected into the chamber by a shaker dispenser. After the particles were trapped in the RF plasma, the DC voltage was turned off. The plasma was then sustained only by 0.4-W power applied to the RF coil. Figure 1(b) shows a snapshot image of the plasma trapping two dust clouds in the vicinity of the RF coil. The two dust clouds locate asymmetrically with respect to the RF coil, presumably due to an asymmetry in plasma conditions such as ion flows and plasma electric fields.

To observe the motion of individual particles, we used two particle observation (PO) cameras with an illumination laser sheet. The two PO cameras were aligned along the axis of the plasma chamber, with a slight overlap of their fields of view. This arrangement almost doubles the total field of view that we can image. A thin slab of particles was illuminated; the motion of the particles was recorded by the cameras at 100 frames per second and 0.0142 mm/pixel resolution. The video images have the dimensions 1600 pixel × 267 pixel. Figure 2(a) shows a snapshot image from one of the PO cameras.

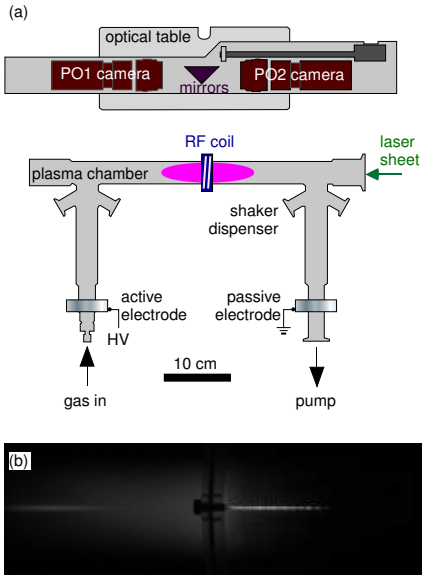

FIG. 1. (Color online) (a) Sketch of PK-4 instrument showing a RF coil positioned near the middle of the U-shaped plasma chamber. The RF coil was powered at radio frequency (RF) to generate a glow-discharge plasma. Dust particles are injected into the chamber by a shaker dispenser; they are confined by the RF plasma. Two particle observation (PO) cameras view a slab of the particles, which is illuminated by a laser sheet. A plasma glow observation (PGO) camera (not shown here) is used to observe the plasma glow, in a larger field of view. (b) Snapshot of a plasma (its glow appears here in a bulk volume with a white color that is faint, due to an optical filter) trapping two dust clouds (the two bright stripes concentrated near the middle line of the image). The image was recorded by the PGO camera, which views the plasma chamber at an angle parallel to the illuminated slab. All our results in Sec. IV are for the dust cloud on the right.

III. DATA ANALYSIS

We performed the analysis of images from the PO cameras two ways, using particle-level and continuum approaches. The particle-level measurements were used to determine the time-average number density of particles as well as the fluctuations in the number density. The continuum approach is one where the collection of dust particles is described locally as a dust fluid.

A. Particle identification

We determined particle position from the image data recorded by the PO cameras. In an image, a particle

appears as a bright spot filling multiple pixel. Using the optimized moment method in [60], a particle's position was calculated as a weighted average of pixel positions. The weight factor here was the intensity of each pixel in the bright spot associated with the particle. Thus, we obtained the x and y positions of particles in each camera frame, with a sub-pixel resolution.

B. Number density of particles

Using the position of individual particles, we determined the number density n_d of dust particles. Here we only use the particles in the ROI 1 marked in Fig. 2(a), where wave activities are relatively low. We first calculated the pair correlation function $g(r)$, yielding the particle spacing 0.38 mm, which is the first peak of the $g(r)$. The number density n_d was then determined using the method in [61]. We found $n_d = 2.6 \times 10^{10}$ m^{-3}, which will be used in our calculation of a theoretical dispersion relation in Sec. IV. Since our dust cloud was not uniform and its density was modulated by DAWs, so the determined number density is essentially an average value.

C. Space-time diagram of dust fluid velocity

We obtained the fluid velocity field in the dust cloud using particle image velocimetry (PIV). Our PIV analysis was performed in three main steps. In the first step, we preprocessed our recorded images by subtracting a background image, which was recorded in the absence of dust particles, and then enhancing the contrast of the resulting images using histogram equalization. In the second step, we divided each image into an array of 2D subareas (called interrogation areas) of dimension 0.625 mm $\times$ 0.625 mm, and then the displacements in the subareas were evaluated using the direct cross correlation [62, 63] of the images from two consecutive video frames. In the third step, we validated our PIV data using the vector difference test and normalized median test [62]. Using these PIV data, we obtained a velocity vector for each subarea at (x, y) and for the time t at the midpoint between the two consecutive frames. In this paper, we only use the x component of the velocity data, $u_x(x, y, t)$.

We prepared the space-time diagram of an averaged dust-fluid velocity $V_x(x, t)$, which was obtained by averaging $u_x(x, y, t)$ over y. This diagram is presented in Fig. 2(b) as a contour plot of $V_x(x, t)$; it is used to characterize wave propagation in our dust cloud. In this diagram, wavefronts appear as periodic stripes, from which we can determine the wavelength, the frequency, and the phase speed of the propagating waves.

D. Correlation function of microscopic particle density

To characterize the collective modes arising from density fluctuations, we obtained a time series of microscopic particle density using

$$\rho(k, t) = \sum_{j=1}^{N} e^{-ikx_j(t)}. \tag{1}$$

Here, the particle density $\rho(k, t)$ was computed for various values of wave number k, using the position x_j of individual particles that we identified. The number of dust particles N here only accounts for the particles identified in the thin slab that was imaged by the PO cameras. We note that our calculation using Eq. (1), which is a spatial Fourier transform of particle's number density, is essentially a decomposition of the density fluctuations (arising from particle's random motion) into harmonic-oscillator-like modes with different length scales (wave numbers). Alternatively, one can use an approach [42] that is based on Hilbert transform, which can yield the variation of wave phase in space and time. The Hilbert approach has been used to characterize dust acoustic waves in a nanodusty plasma [42], yielding spatially-resolved plasma parameters.

Our experimental density correlation function was calculated using

$$F(k, \tau) = \langle \rho(k, t_0 + \tau)\rho(k, t_0) \rangle / N, \tag{2}$$

for each wave number k. Here, τ is the time delay from a time zero t_0; we chose multiple time zeros at 0.05-s intervals in the time series of $\rho(k, t)$. The brackets $\langle \ldots \rangle$ represent a time average over different time zero t_0. Figure 4 shows examples of the correlation function.

E. Wave spectrum

The wave spectrum was calculated as

$$S(k, f) = |\rho(k, f)|^2 / N, \tag{3}$$

which is the power spectral density (PSD) of $\rho(k, t)$, as a function of the wave number k and the frequency f. Here $\rho(k, f)$ is calculated by Fourier transforming the time series of $\rho(k, t)$. The wave spectrum $S(k, f)$ is also called a dynamic structure factor in the physics of liquids [64]. Figure 5(a) is our result for the wave spectrum, which is presented as a contour plot of $S(k, f)$ in terms of k and f.

IV. RESULTS

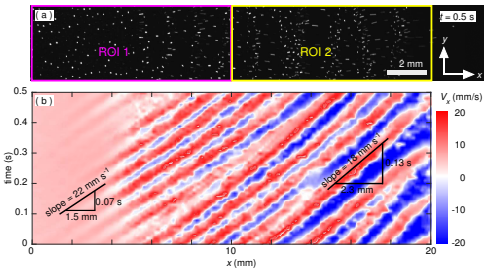

FIG. 2. (Color online) (a) Snapshot image of a dust cloud, as recorded by one of the PO cameras. Density compression and rarefaction are seen from the variation of image pixel brightness. (b) Space-time diagram of dust fluid velocity $V_x(x,t)$, for the dust motion in the direction of ion flow. This velocity was obtained by averaging velocity data $u_x(x,y,t)$, which was evaluated using particle image velocimetry (PIV). The stripe features in (b) represent wavefronts that propagate in space and time. The waves here are dust acoustic waves, and they propagate from left to right, and their amplitude grows as they propagate, with a larger amplitude in region-of-interest ROI 2 than in ROI 1.

A. Dust acoustic waves (DAWs)

In the experiment, we observed DAWs self-exciting in our dusty plasma under microgravity conditions. The waves were generated spontaneously as the gas pressure was reduced to about 35 Pa; they were self-sustained, without any external manipulation. The waves were steady in time and long-lived, because the particles were trapped in an RF plasma. Figure 2(a) is a snapshot showing a series of density compression and rarefaction, which propagated in the $+x$ direction, i.e., the direction of ion flow. We note that this experiment differed from a previous ISS PK-4 experiment [54, 55], where DAWs were excited in a dust cloud that was drifting in a DC plasma; our cloud was not drifting, because we used an RF-powered plasma to trap it.

We find dominant modes for the DAWs. This can be seen from the space-time diagram of dust-fluid velocity in Fig. 2(b). For the mode at small x, the wavefronts exhibit a frequency of about $f = 15$ Hz and a wavelength of 1.5 mm (or wave number $k = 4.4$ mm^{-1}), with a phase speed of 22 mm s^{-1}. The mode observed at large x has a wavelength of 2.3 mm (or $k = 2.7$ mm^{-1}) and $f = 7.7$ Hz, with a phase speed of 18 mm s^{-1}. The obtained phase speeds are comparable to those found in the previous PK-4 experiment [54], although a different plasma was used in that experiment.

We also note that the waves grew as they propagated in the $+x$ direction. In Fig. 2(b), the amplitude of the fluid velocity shows an overall increase with x. The amplitude varies from ≈ 5 mm s^{-1} at small x to ≈ 30 mm s^{-1} at large x. Furthermore, we have also checked the waveforms (i.e., the time series of the number density of particles) at two locations $x = 6.5$ and 16.5 mm, in Figs. 3(a) and 3(b), respectively. The time series was calculated by averaging pixel intensity in a vertical bin of the width 0.14 mm, for video frames such as that in Fig. 2(a). We fit the experimental waveforms to cnoidal functions as in Ref. [43], yielding a nonlinearity measure m, which is called the elliptic parameter characterizing the shapes of cnoidal functions. Our fitted value in Fig. 3(a), $m = 0.34$, indicates that the waves are weakly nonlinear in ROI 1, as compared with $m = 0$ for a cosine function. At large x in ROI 2, the waves become strongly nonlinear, with $m = 0.76$, as also seen from the sharpened peaks and flatten bottoms in the waveforms, Fig. 3(b). We note that the nonlinearity in our microgravity experiment here is weaker than that for a ground-based experiment [43], where a large value of $m \approx 1$ was observed for a dust cloud levitating in a plasma sheath.

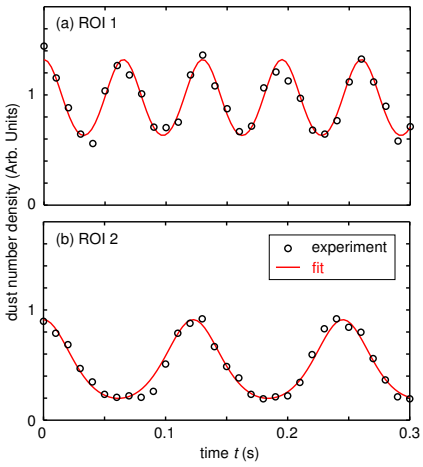

FIG. 3. (Color online) Experimental waveforms of the number density of dust particles (circles). The data were obtained by calculating the time series of pixel intensity of images such as that in Fig. 2(a), at two locations: (a) $x = 7.5$ mm in ROI 1 and (b) $x = 16.5$ mm in ROI 2. The waveforms in (b) exhibit sharpened peaks and flatten bottoms, indicating the waves are strongly nonlinear. To characterize the nonlinearity of waves, the experimental waveforms were fitted to cnoidal functions (the continuous curves) using Eq. (3) in Ref. [43], yielding a nonlinear measure m. The parameter m has a possible value ranging from zero to unity. The sharpened peaks and flattened bottoms of the waveforms in (b) are characterized by a larger value $m = 0.76$.

Since the waves grew in the $+x$ direction and exhibited different degree of nonlinearity at different x location, hereafter we will discuss our results in two regions-of-interest (ROIs). The ROIs are marked in Fig. 2(a), with ROI 1 for $0 < x \leq 10$ mm and ROI 2 for $10 < x \leq 20$ mm. We have also verified that wave frequency does

not exhibit significant spatial variation within each ROI, although the frequency does exhibit a transition across the boundary region between the two ROIs.

The temporal decay of the modes is characterized using density correlation functions, Fig. 4. We obtained the correlation data separately in the two ROIs. Figure 4(a) shows the correlation-function data in ROI 1 for wave number $k = 4.4$ mm^{-1}, while Fig. 4(b) is for $k = 2.7$ mm^{-1} in ROI 2.

The correlation functions exhibit both oscillations and decay. To quantify this behavior, we fit the experimental correlation function to the expression [65]

$$C(k,t) \propto e^{-\nu_k t/2}[\cos(2\pi f_k t) + \frac{\nu_k}{4\pi f_k}\sin(2\pi f_k t)]. \quad (4)$$

The fitting yields two parameters: the frequency f_k and the decay rate ν_k, for each mode k. The variation of f_k with k is our measurement of the dispersion relation for the waves.

The oscillation and decay of the correlation function in Fig. 4 were fit to Eq. (4). This yielded the decay rate $\nu_k = 8.3$ s^{-1} and the frequency $f_k = 15.1$ Hz, for $k = 4.4$ mm^{-1} in ROI 1, where the wave propagation is first seen. We similarly obtained $\nu_k = 8.7$ s^{-1} and $f_k = 7.9$ Hz, for $k = 2.7$ mm^{-1} in ROI 2, where the waves have propagated after exiting ROI 1. We find that the measured decay rate is much smaller than the gas damping rate, $\nu_d = 38.5$ s^{-1}, as calculated using the Epstein's formula [61]. If there were not any external energy input to the waves, one would expect the waves to decay at least as fast as the gas damping rate. However, the smaller decay rate observed here indicates that the waves gained energy as they propagated. The energy source must have been from ion flows.

The decay of the correlation can be thought of as a decorrelation, which is essentially a 'forgetting' process regarding the wave's phase coherence. The wave gradually forgets what phase and frequency it would be expected to have, based on the way it was oscillating earlier. This decorrelation can arise from several possible mechanisms, including unsteady wave excitations, and nonlinear wave interactions such as wave-front merging [31, 38–40, 49], which can cause energy to cascade from a mode at one wavelength and frequency to another.

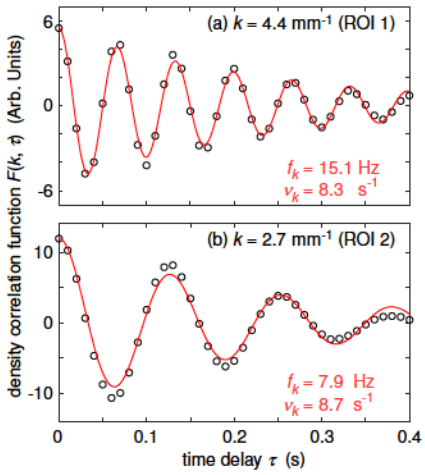

FIG. 4. (Color online) Density correlation functions showing decaying oscillations. The circle symbols are experimental measurement, as obtained using Eqs. (1) and (2) with the particle position data. The continuous curves are fits to the data using Eq. (4) with two free parameters: the frequency f_k and the decay rate ν_k. The data shown here are for two modes: (a) $k = 4.4$ mm^{-1} in ROI 1 and (b) $k = 2.7$ mm^{-1} in ROI 2.

B. Wave spectrum

Here we explore collective modes in a broad range of wave numbers. We will present our results for a wave spectrum, which is calculated for ROI 1. We choose ROI 1 because the waves were not strongly nonlinear there.

Figure 5(a) shows our result for the wave spectrum, which is the power spectral density as a function of wave number and wave frequency. A major feature of this spectrum is a distinctive frequency band running from lower left corner to upper right corner of this graph. This band represents high concentration of spectral power.

The hot spot at $k = 4.4$ mm^{-1} in the spectrum represents a concentration of spectral power. To reveal this feature better, we present Fig. 5(b), which is a graph of the power spectral density distribution versus wave number. This graph was obtained by integrating the spectrum in Fig. 5(a) over frequency. We note that this concentration is unlike the random motion in equilibrium systems, where equipartition among modes is expected.

For ROI 1, this concentration of spectral power in Figs. 5(a) and 5(b) corresponds to the feature in Fig. 2(b) that we described as the dominant mode, also for ROI 1. While the space-time diagram (which was prepared for a short time range) revealed a mode with well-defined frequency and wave number at a given moment, the spectrum (which was for a longer time range) shows a range of modes ($3 < k < 5$ mm^{-1}). This broadening in the range may suggest the existence of fluctuations in mode excitation. In general, energy is mostly injected into a most unstable mode at a wave number determined by the plasma instability driven by the nonequilibrium presence of flowing ions. However, fluctuations in plasma conditions could cause the mode's wave number and frequency to deviate from an average value, leading to the broadening of the range of the exited wave number and frequency.

Our results in Figs. 5(a) and 5(b) also indicate the

emergence of a broader spectrum of harmonic modes, well-beyond the hot spot. The wave spectrum Fig. 5(a) reveals a broad distribution of spectral power spanning almost all wave numbers in the range shown, although the power spectral density in Fig. 5(b) is not equally partitioned among the modes. There might be some mechanisms (e.g. nonlinear coupling) that could transfer energy from the hot spot to other modes. These modes are not entirely coherent, i.e., they are random in nature, as indicated by the decay of correlation functions. For the modes $k > 6$ mm^{-1}, the decay rate is faster than that due to gas damping, Fig. 5(c).

C. Dispersion relation

Here we describe the waves in ROI 1 as obeying a dispersion relation. Generally, dispersion relations are used for low-amplitude waves exhibiting linear behavior. Although the waves in our experiment were nonlinear, the degree of nonlinearity in ROI 1 was not great. Indeed, we find here that for ROI 1, using the correlation function fitting results as in Fig. 4, we are able to obtain an experimental dispersion relation.

Our measurement of the real part of the dispersion relation is indicated by circle symbols in Fig. 5(a). The fitting also yielded the measurement of the decay rate ν_k, Fig. 5(c). All data are shown, except for those with small k where the correlation function does not fit well to Eq. (4).

For comparison, we also obtain a linear dispersion relation using a kinetic model [13]. This dispersion relation includes the effects such as charge separation, ion drift, electron-neutral collisions, ion-neutral collisions, dust-neutral collisions, and so on. The real and imaginary parts of the dispersion relation, $\omega(k) = 2\pi f_r(k) + i\omega_{im}(k)$, are calculated using Eq. (2) in [13], which is

$$1 + \sum_\alpha \frac{1}{(k\lambda_{D\alpha})^2} \frac{1 + \xi_\alpha Z(\xi_\alpha)}{[1 + (i\nu_\alpha/\sqrt{2}kV_{T\alpha})Z(\xi_\alpha)]} = 0, \quad (5)$$

where $\alpha = e, i, d$ for the electron, ion, and dust components, respectively. For each component, the input parameters for the theory include the component's temperature T_α, charge Q_α, number density n_α, and mass m_α. We calculate $\lambda_{D\alpha} = (\epsilon_0 k_B T_\alpha / Q_\alpha^2 n_\alpha)^{1/2}$, the thermal velocity $V_{T\alpha} = (k_B T_\alpha / m_\alpha)^{1/2}$, and the collision rate ν_α between the component and neutral atoms. Here, $Z(\xi_\alpha)$ is the plasma dispersion function, with

$$\xi_d = \frac{\omega + i\nu_d}{\sqrt{2}kV_{Td}}, \; \xi_e = \frac{\omega + i\nu_e}{\sqrt{2}kV_{Te}}, \; \xi_i = \frac{\omega - kU_0 + i\nu_i}{\sqrt{2}kV_{Ti}}. \quad (6)$$

The ion drift velocity U_0 is calculated using $U_0 = \mu_+ E_{dc}$ with Frost's ion mobility μ_+ [66], in an electric field E_{dc}. The ion-neutral collision rate ν_i is estimated as $\nu_i = e/m_i\mu_+$. The electron-neutral collision rate ν_e is estimated as $\nu_e = n_n \sigma V_{Te}$, where the cross-section $\sigma = 2.144 \times 10^{-16}$ cm^{-2} is obtained from [67] and n_n is

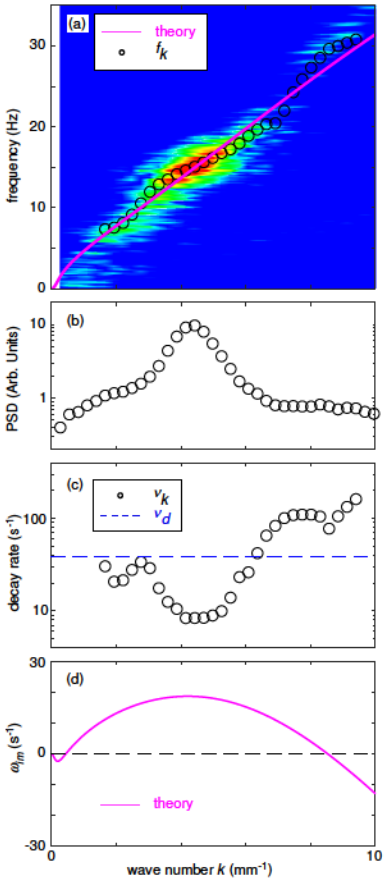

FIG. 5. (Color online) Characterizing the collective modes arising from spontaneous fluctuations. All the experimental data shown here are for ROI 1 only. (a) Wave spectrum (filled contours), along with the real part of the dispersion relation: experimental measurement f_k (circle symbols) and theoretical prediction (continuous curve). The wave spectrum was calculated using Eqs. (1) and (3) with the particle position data. The data points for f_k were from fitting the correlation functions as in Fig. 4. The theoretical curve was calculated using Eq. (5), which is a linear theory for DAWs [13]. The experimental and theoretical dispersion relations exhibit a general agreement. (b) Power spectral density (PSD) variation with wave number. The PSD was computed by integrating the spectrum in Fig. 5(a) over frequency. The peak near $k = 4.4$ mm^{-1} corresponds to the dominant DAW mode in ROI 1. (c) Decay rate ν_k showing a minimum near the dominant mode. The data points for ν_k were from fitting the correlation functions as in Fig. 4. The dashed line indicates the damping rate due to gas friction. Even though DAWs were excited continuously, they were not entirely coherent as indicated by the finite value of the decay rate. (d) Imaginary part of the theoretical dispersion relation (solid curve).

TABLE I. Input parameters for the calculation of the theoretical dispersion relation.

Parameter	Value		Comment
n_d	2.6×10^{10}	m^{-3}	measured using $g(r)$
V_d	5.8	mm s^{-1}	measured using the data in Fig. 2(b)
T_i	300	K	assumed
μ_+	9651	cm^2/V s	mobility from Frost [a]
Q_d	7470 ± 1800	e	calculated using OML model
n_e	$(1.5 \pm 1.4) \times 10^{14}$	m^{-3}	$n_e = n_i - Q_d n_d$
n_i	$(3.5 \pm 1.9) \times 10^{14}$	m^{-3}	fitted
T_e	1.6 ± 0.4	eV	fitted
E_{dc}	4.8 ± 0.6	V cm^{-1}	fitted
T_d	71 ± 28	eV	fitted

[a] Ref. [66]

the neutral gas density. The dust-neutral collision rate ν_d uses the value for the Epstein damping rate, 38.5 s^{-1}, as calculated earlier.

To compare to our experiment, we also consider the effect of the dust flow velocity V_d. The theoretical dispersion relation from Eq. (5) is derived in a moving frame with dust, which in our experiment exhibited an overall drift $V_d = 5.8$ mm s^{-1} in ROI 1. As in Ref. [55], we take into account this drift by adding an additional term to the real part $f_r(k)$ from Eq. (5), yielding the dispersion in the laboratory reference frame

$$f(k) = f_r(k) + kV_d/2\pi. \tag{7}$$

An experimental measurement of the flow velocity V_d was obtained by averaging the instantaneous fluid velocity in ROI 1 of Fig. 2(b) over a 10-s interval.

We present our calculated dispersion relation in Figs. 5(a) and 5(d). The continuous curve in Fig. 5(a) is the real part of the dispersion relation calculated using Eq. (5) with the input parameters listed in Table I. In obtaining this curve, we fit the experimental data points in Fig. 5(a) using Eq. (5), with four free parameters: n_i, T_e, T_d, and E_{dc}. This fit also ensures the imaginary part in Fig. 5(d) has its maximum near the peak in the data for the PSD in Fig. 5(b). The uncertainty of the fitted parameters was obtained by using the Bootstrap method [68]. The value for the kinetic temperature of the dust particles obtained by fitting was $T_d = 71$ eV. We note that this value corresponds to a dust speed of merely 3 mm s^{-1}, which is well within the range of dust fluid velocity in Fig. 2(b). (It is actually common, in dusty plasmas, for kinetic temperatures of dust particles to greatly exceed the temperatures of neutral gas and other plasma constituents, and this is possible because of the large mass of a particle, in comparison to the other constituents.)

The real part of the analytical dispersion relation in Fig. 5(a) coincides with that from our experiment. They both follow an acoustic-wave-like uptrend. We do not expect a perfect agreement, because the waves in our experiment were not entirely linear while the theoretical model is for linear waves. Nevertheless, the agreement in Fig. 5(a) is remarkable.

For the imaginary part of the dispersion relation, ω_{im}, we can test the theoretical prediction of the most unstable modes. By making sure that the maximum of the imaginary part in Fig. 5(d) coincides with the peak in the PSD in Fig. 5(b), we verified the theoretical prediction of wave excitation. However, we note that we are unable to test the magnitude of the imaginary part, because we do not have an experimental measurement of the imaginary part. The decay rate ν_k that we obtained from the correlation functions may be affected not only by wave damping in the linear sense, but also by nonlinear processes such as wavefronts merging as well as unsteady phase conditions in the excitation region.

D. Conclusion

We presented a microgravity experiment using the ESA-Roscosmos facility PK-4 on the ISS, investigating dust acoustic waves in plasmas. A 3D cloud of charged microspheres was confined in an inductively-coupled radio-frequency glow discharge plasma, which was prepared using low-pressure neon gas. The correlation function of the DAWs exhibits a decaying oscillation. The decay rate is much slower than the gas damping rate, suggesting energy injection to the waves. The wave spectrum of density fluctuations indicates the emergence of collective vibration modes in a broad range of wave numbers. These modes follow a dispersion relation, which can fit a linear theory, based on a kinetic model.

ACKNOWLEDGMENTS

All authors acknowledge the joint ESA/Roscosmos "Experiment Plasmakristall-4" onboard the International Space Station. Work was partially supported by DLR Grant Nos. 50WM1441 and 50WM1742. A. M. Lipaev and A. D. Usachev were supported by the Russian Science Foundation (Project No. 20-12-00365). Work at Iowa was supported by NASA-JPL subcontracts 1573629 and 1579454, and NSF Award No. 1740379. Work at Auburn was supported by NASA-JPL subcontract 1571699 and NSF Award No. PHY-1740784.

DATA AVAILABILITY

The data that supports the findings of this study are available within the article.

[1] J. H. Chu and L. I, Phys. Rev. Lett. **72**, 4009 (1994).
[2] H. Thomas, G. E. Morfill, V. Demmel, J. Goree, B. Feuerbacher, and D. Mohlmann, Phys. Rev. Lett. **73**, 652 (1994).
[3] Y. Hayashi and K. Tachibana, Jpn. J. Appl. Phys. **33**, L804 (1994).
[4] A. Melzer, A. Homann, and A. Piel, Phys. Rev. E **53**, 2757 (1996).
[5] H. M. Thomas and G. E. Morfill, Nature **379**, 806 (1996).
[6] A. Homann, A. Melzer, S. Peters, R. Madani, and A. Piel, Phys. Lett. **242**, 173 (1998).
[7] A. Piel, A. Homann, and A. Melzer, Plasma Phys. Control. Fusion **41**, A453 (1999).
[8] B. Liu, K. Avinash, and J. Goree, Phys. Rev. Lett. **91**, 255003 (2003).
[9] A. Melzer, *Waves in strongly coupled dusty plasmas* in *Physics of Dusty Plasmas*, Lecture Notes in Physics **962**, (Springer, Cham, 2019), p. 115.
[10] S. Nunomura, J. Goree, S. Hu, X. Wang, A. Bhattacharjee, and K. Avinash, Phys. Rev. Lett. **89**, 035001 (2002).
[11] B. Liu and J. Goree, Phys. Rev. E **71**, 046410 (2005).
[12] N. N. Rao, P. K. Shukla, and M. N. Yu, Planet. Space Sci. **38**, 543 (1990).
[13] M. Rosenberg, J. Vac. Sci. Technol. A **14**, 631 (1996).
[14] R. L. Merlino, A. Barkan, C. Thompson, and N. D'Angelo, Phys. Plasmas **5**, 1607 (1998).
[15] V. V. Yaroshenko, S. A. Khrapak, H. M. Thomas, and G. E. Morfill, Phys. Plasmas **19**, 023702 (2012).
[16] R. L. Merlino, J. Plasma Phys. **80**, 773 (2014).
[17] A. Melzer, *Waves in weakly coupled dusty plasmas* in *Physics of Dusty Plasmas*, Lecture Notes in Physics **962**, (Springer, Cham, 2019), p. 101.
[18] J. H. Chu, J.-B. Du, and L. I, J. Phys. D: Appl. Phys. **27**, 296 (1994).
[19] A. Barkan, R. L. Merlino, and N. D'Angelo, Phys. Plasmas **2**, 3563 (1995).
[20] C. Thompson, A. Barkan, N. D'Angelo, and R. L. Merlino, Phys. Plasmas **4**, 2331 (1997).
[21] V. I. Molotkov, A. P. Nefedov, V. M. Torchinskii, V. E. Fortov, and A. G. Khrapak, JETP **89**, 477 (1999).
[22] V. E. Fortov, A. G. Khrapak, S. A. Khrapak, V. I. Molotkov, A. P. Nefedov, O. F. Petrov, and V. M. Torchinsky, Phys. Plasmas **7**, 1374 (2000).
[23] E. Thomas Jr. and R. L. Merlino, IEEE Trans. Plasma Sci. **29**, 152 (2001).
[24] J. Pramanik, B. M. Veeresha, G. Prasad, A. Sen, and P. K. Kaw, Phys. Letts. A **312**, 84 (2003).
[25] V. E. Fortov, A. D. Usachev, A. V. Zobnin, V. I. Molotkov, and O. F. Petrov, Phys. Plasma **10**, 1199 (2003).
[26] E. Thomas, Jr., Phys. Plasmas **13**, 042107 (2006).
[27] M. Schwabe, M. Rubin-Zuzic, S. Zhdanov, H. M. Thomas, and G. E. Morfill, Phys. Rev. Lett. **99**, 095002 (2007).
[28] E. Thomas Jr., R. Fisher, and R. L. Merlino, Phys. Plasmas **14**, 123701 (2007).
[29] M. Rosenberg, E. Thomas, Jr., and R. L. Merlino, Phys. Plasmas **15**, 073701 (2008).
[30] J. D. Williams, E. Thomas, and L. Marcus, Phys. Plasmas **15**, 043704 (2008).
[31] I. Pilch, T. Reichstein, and A. Piel, Phys. Plasmas **16**, 123709 (2009).
[32] L.-W. Teng, M.-C. Chang, Y.-P. Tseng, and Lin I, Phys. Rev. Lett. **103**, 245005 (2009).
[33] V. Nosenko, S. K. Zhdanov, S.-H. Kim, J. Heinrich, R. L. Merlino, and G. E. Morfill, EPL **88**, 65001 (2009).
[34] T. M. Flanagan and J. Goree, Phys. Plasmas **17**, 123702 (2010).
[35] J. D. Williams and E. K. Snipes, IEEE Trans. Plasma Sci. **38**, 847(2010).
[36] E. Thomas Jr., Phys. Plasmas **17**, 043701 (2010).
[37] J. D. Williams and J. Duff, Phys. Plasmas **17**, 033702 (2012).
[38] J. D. Williams, IEEE Trans. Plasmas **41**, 788 (2013).
[39] M.-C. Chang, Y.-Y. Tsai, and L. I, Phys. Plasmas **20**, 083703 (2013).
[40] W. D. Suranga Ruhunusiria and J. Goree, IEEE Trans. Plasma Sci. **42**, 2688 (2014).
[41] W. D. Suranga Ruhunusiria and J. Goree, Phys. Plasmas **21**, 053702 (2014).
[42] B. Tadsen, F. Greiner, S. Groth, and A. Piel, Phys. Plasmas **22**, 113701 (2015).
[43] B. Liu, J. Goree, T. M. Flanagan, A. Sen, S. K. Tiwari, G. Ganguli, and C. Crabtree, Phys. Plasmas **25**, 113701 (2018).
[44] J. Williams, IEEE Trans. Plasma Sci. **47**, 3107 (2019).
[45] A. Melzer, H. Kruger, S. Schutt, and M. Mulsow, Phys. Plasmas **27**, 033704 (2020).
[46] A. Piel, M. Klindworth, O. Arp, A. Melzer, and M. Wolter, Phys. Rev. Lett. **97**, 205009 (2006).
[47] O. Arp, D. Caliebe, K. O. Menzel, A. Piel, and J. Goree, IEEE Trans. Plasma Sci. **38**, 842 (2010).
[48] K. O. Menzel, O. Arp, and A. Piel, Phys. Rev. Lett. **104**, 235002 (2010).
[49] K. O. Menzel, O. Arp, and A. Piel, Phys. Rev. E **83**, 016402 (2011).
[50] S. Khrapak, D. Samsonov, G. Morfill, H. Thomas, V. Yaroshenko, H. Rothermel, T. Hagl, V. Fortov, A. Nefedov, and V. Molotkov et al., Phys. Plasmas **10**, 1 (2003).
[51] V. V. Yaroshenko, B. M. Annaratone, S. A. Khrapak, H. M. Thomas, G. E. Morfill, V. E. Fortov, A. M. Lipaev, V. I. Molotkov, O. F. Petrov, A. I. Ivanov, and M. V. Turin, Phys. Rev. E **69**, 066401 (2004).
[52] M. Schwabe, S. K. Zhdanov, H. M. Thomas, A. V. Ivlev, M. Rubin-Zuzic, G. E. Morfill, V. I. Molotkov, A. M. Lipaev, V. E. Fortov, and T. Reiter, New J. Phys. **10**, 033037 (2008).

[53] H. M. Thomas, M. Schwabe, M. Y. Pustylnik, C. A. Knapek, V. I. Molotkov, A. M. Lipaev, O. F. Petrov, V. E. Fortov, and S. A. Khrapak, Plasma Phys. Control. Fusion **61**, 014004 (2019).
[54] S. Jaiswal, M. Y. Pustylnik, S. Zhdanov, H. M. Thomas, A. M. Lipaev, A. D. Usachev, V. I. Molotkov, V. E. Fortov, M. H. Thoma, and O. V. Novitskii, Phys. Plasmas **25**, 083705 (2018).
[55] V. V. Yaroshenko, S. A. Khrapak, M. Y. Pustylnik, H. M. Thomas, S. Jaiswal, A. M. Lipaev, A. D. Usachev, O. F. Petrov, and V. E. Fortov, Phys. Plasmas **26**, 053702 (2019).
[56] A. P. Nefedov, G. E. Morfill, V. E. Fortov, H. M. Thomas, H. Rothermel, T. Hagl, A. V. Ivlev, M. Zuzic, B. A. Klumov, A. M. Lipaev, and V. I. Molotkov et al., New J. Phys. **5**, 33.1 (2003).
[57] H. M. Thomas, G. E. Morfill, V. E. Fortov, A. V. Ivlev, V. I. Molotkov, A. M. Lipaev, T. Hagl, H. Rothermel, S. A. Khrapak, and R. K. Suetterlin et al., New J. Phys. **10**, 033036 (2008).
[58] M. Y. Pustylnik, M. A. Fink, V. Nosenko, T. Antonova, T. Hagl, H. M. Thomas, A. V. Zobnin, A. M. Lipaev, A. D. Usachev, and V. I. Molotkov et al., Rev. Sci. Instrum. **87**, 093505 (2016).
[59] A. D. Usachev, A. V. Zobnin, A. V. Shonenkov, A. M. Lipaev, V. I. Molotkov, O. F. Petrov, V. E. Fortov, M. Y. Pustylnik, M. A. Fink, M. A. Thoma, H. M. Thomas, and G. I. Padalka, J. Phys: Conf. Series **946**, 012143 (2018).
[60] Y. Feng, J. Goree, and Bin Liu, Rev. Sci. Instrum. **78**, 053704 (2007).
[61] B. Liu, J. Goree, and W. D. Suranga Ruhunusiri, Rev. Sci. Instrum. **86**, 033703 (2015).
[62] M. Raffel, C. E. Willert, F. Scarano, C. J. Kähler, S. T. Wereley, and J. Kompenhans, *Particle Image Velocimetry: A Practical Guide*, 3rd ed., (Springer, Cham, 2018).
[63] W. Thielicke and E. J. Stamhuis, J. Open Res. Softw. **2**, e30 (2014). DOI: http://doi.org/10.5334/jors.bl
[64] J.-P. Hansen and I. R. McDonald, *Theory of simple liquids*, 3rd ed., Academic Press, Cambridge, 2006, p. 199.
[65] W. T. Coeffey and Y. P. Kalmykov, *The Langevin equation: with applications to stochastic problems in physics, chemistry and electrical engineering*, 4th ed., World Scientific, Singapore, 2017, p. 283.
[66] L. S. Frost, Phys. Rev. **105**, 354 (1957).
[67] A. G. Robertson, J. Phys. B: Atom. Molec. Phys. **5**, 648 (1972).
[68] W. H. Press, S. A. Teukolsky, W. T.Vetterling, and B. P. Flannery, *Numerical recipes in FORTRAN: the art of scientific computing*, 2nd ed., University Press, Cambridge, 1992, p. 686.

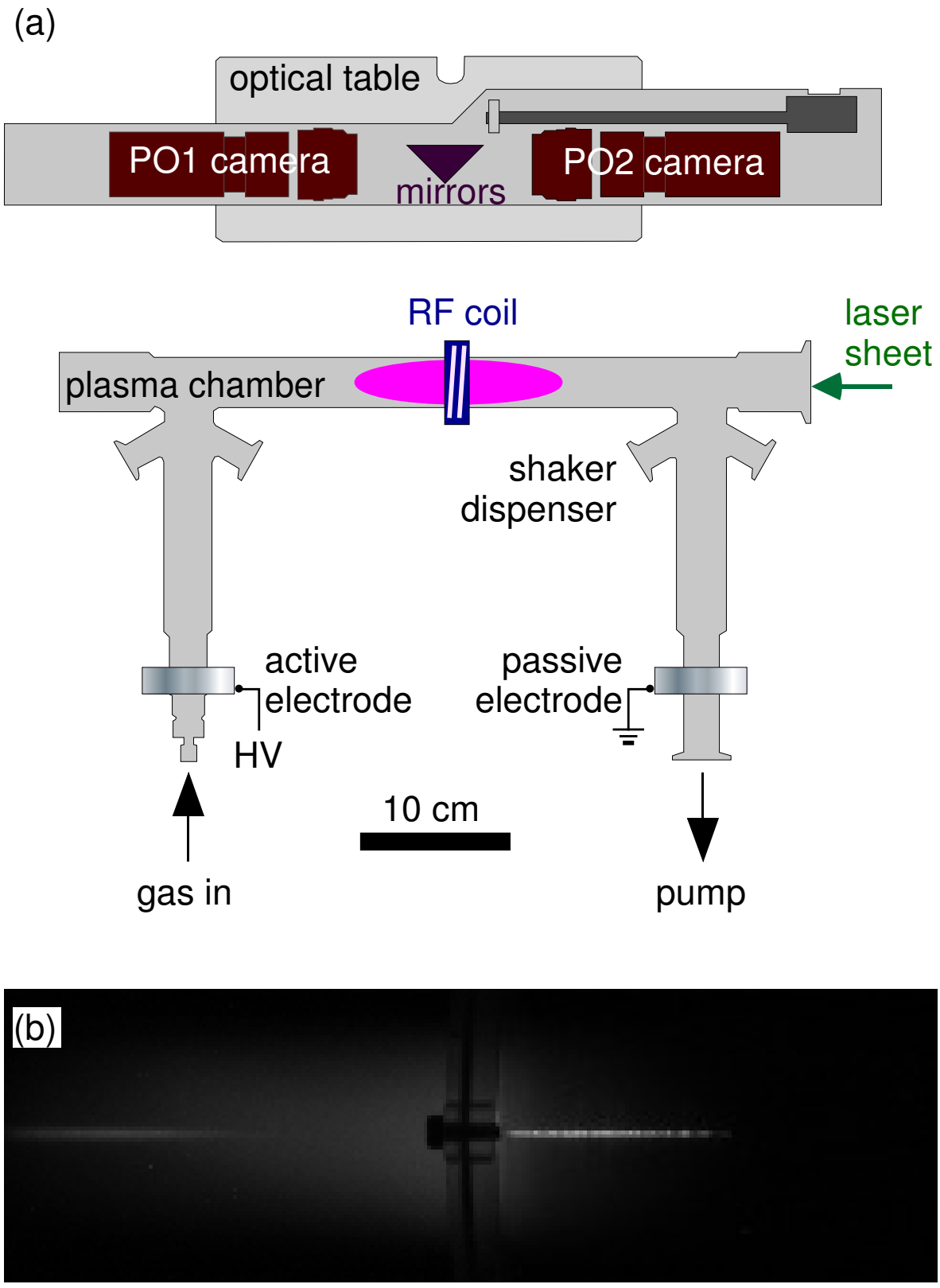

Physics of Plasmas